Effects of motion in sparsely sampled acquisitions

18

Sajan Goud Lingala[a,b] **and Rushdi Zahid Rusho**[a]

[a]*Roy J Carver Department of Biomedical Engineering, University of Iowa, Iowa City, IA, United States*
[b]*Department of Radiology, University of Iowa, Iowa City, IA, United States*

18.1 Introduction

Sparsely sampled acquisitions coupled with constrained reconstruction are commonly used in several MR applications to address the fundamental imaging trade-offs between resolution, coverage, signal-to-noise ratio, and scan time. In this chapter, we focus on the effects of motion in such schemes. We will consider motion in the context of interframe movement in dynamic imaging applications (e.g., cardiac motion in myocardial cine MRI, breathing motion in free-breathing pulmonary MRI, vocal tract movement in dynamic speech MRI). We will begin by discussing the effects of motion and analyzing artifacts due to choice of k-space versus time sampling patterns, while using classic linear sliding window reconstruction. We will then highlight the advantages of non-Cartesian sampling schemes to efficiently encode motion. Practical challenges associated with non-Cartesian sampling will be discussed (e.g., need for trajectory error corrections with radial sampling, sensitivity to off-resonance artifacts with spiral sampling).

We will then focus on reconstructions that exploit spatiotemporal redundancies in the dynamic dataset. We will begin by discussing generalized spatiotemporal models and how they model motion. These include schemes based on leveraging (a) structure/sparsity under predetermined transforms (e.g., compressed sensing), (b) low-rank structure of the dynamic data, and (c) sparsity under dictionaries learned from the data itself. We will highlight challenges associated with these schemes in accurately representing various patterns of motion. Next, we will focus on explicit motion estimation and compensation reconstruction schemes, which have shown tremendous promise in minimizing motion artifacts associated with classic spatiotemporal models. We will also discuss implicit motion compensation methods, where strategies based on heuristics such as data sorting, motion binning based on navigator signals (i.e., "extra dimension" class of methods). Next, we will show examples from emerging manifold regularization schemes, which allow for implicit motion compensation when data binning fails especially with arbitrary motion patterns (e.g., vocal tract movements in dynamic speech MRI). Finally, we will highlight the importance of validation studies needed for standardizing the use of nonlinear model-based constrained reconstruction methods.

18.2 Choice of k-space versus time sampling

18.2.1 Phantom simulation

The choice of k-space versus time sampling pattern plays a critical role when encoding motion. To illustrate this, we compare four k-space versus time sampling schemes in two dynamic MR imaging scenarios in Figs. 18.1 and 18.2. The dynamic MR imaging scenarios involve a circular object experiencing (a) slow position change (akin to slow movement of a catheter in interventional MRI) and (b) shape change (akin to organ shape change such as the beating heart in cardiac cine MRI). Given an acceleration factor of $R = 4$, we compare the below sampling schemes:

- *Lattice sampling*: The first frame has every Rth phase encode sampled, and in subsequent frames, the sampling pattern is circular shifted along the phase encode direction by a single step.
- *Fluoroscopy sampling*: The first frame acquires a $(1/R)$th fraction of the total number of phase encodes. Subsequent frames involve shifting of the previous frame's sampling pattern by a step size of $(1/R)$th phase encodes.
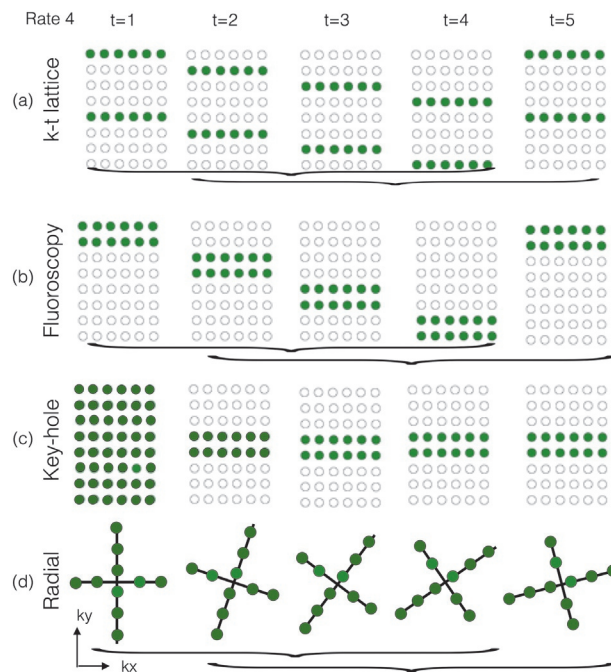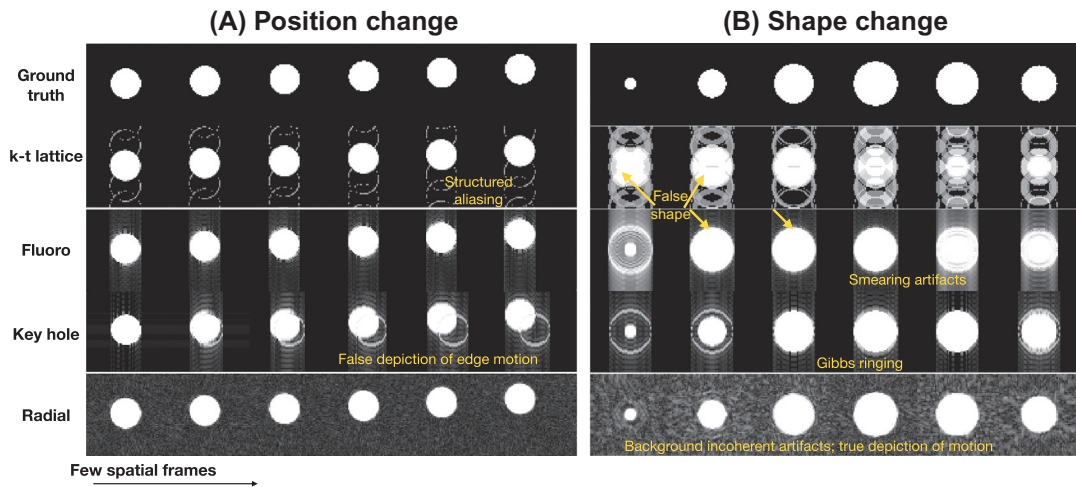

FIG. 18.1

The four k-space versus time sampling schemes used for the phantom simulation in Fig. 18.2: (a) k-t lattice, (b) fluoroscopy, (c) key hole, and (d) radial sampling schemes. *Green shaded circles* indicate the sampled points. Acceleration factor (R) of 4 was simulated. Sliding window reconstruction was used to form an image by combining successive four time instances.

FIG. 18.2

Sliding window reconstructions with different k-t sampling schemes in a dynamic MRI phantom experiment simulating (a) position change and (b) shape change. k-t lattice is observed to produce coherent artifacts, which are strong in the shape change simulation. Fluoroscopy encodes motion in the position change simulation well, but exhibits significant smearing artifact, and false shape depiction in the shape change phantom. Keyhole sampling exhibits classic Gibbs ringing artifacts, and also false depiction of motion of high spatial frequencies (e.g., edges). In contrast, the radial scheme encodes the underlying true motion in both (a) and (b) with good fidelity.

- *Keyhole sampling*: The first frame is fully sampled. The remaining frames sample the central $(1/R)$ th of the k-space.
- *Radial sampling*: Each frame acquires samples on a radial trajectory. The ordering of the spokes may be uniform or follow other patterns such as angular increments following the golden angle (of ≈ 111.25 degrees).

In Figs. 18.1 and 18.2, we use a sliding window reconstruction approach, where k-space samples from consecutive R time frames are combined to form an image. A slide length of 1 frame is used. Sliding window reconstruction is applied for all the sampling patterns except keyhole sampling. In keyhole sampling, images at every frame are formed by combining the high-frequency outer $(1 - 1/R)$th of the k-space from the reference first frame with the low-frequency $(1/R)$th of the k-space of the current frame.

From Fig. 18.2, it can be observed that (a) lattice sampling produces coherent motion artifacts, which get very strong in the shape change simulation; (b) fluoroscopy produces smearing artifacts and tracks the slow motion of the object in position change simulation, but produces false shapes in the fast shape change simulation; (c) keyhole sampling produces Gibbs ringing and depicts the overall motion well in both the simulations, but falsely depicts motion of high-frequency edges as stationary; and (d) radial sampling produces incoherent noise-like artifacts in the background, but is very robust to the motion patterns, and encodes motion well in both scenarios.

18.2.2 Challenges associated with non-Cartesian sampling

Non-Cartesian sampling offers superior motion encoding properties as demonstrated in the above simulation. However, there are several practical considerations that should be taken into account while using these sampling schemes. Radial sampling for instance is sensitive to trajectory mismatch errors, where the actual scanner executed radial trajectory does not match the designed trajectory. This can occur due to various factors such as gradient delays, eddy currents, and nonideal gradient amplifier characteristics. The errors can cause severe image distortions. There are several robust methods to correct these errors including field monitoring probes to measure the executed trajectory, and estimation of trajectories via model-based reconstruction among others. Fig. 18.3 shows one example from a recent structured low-rank matrix completion algorithm [1] that corrects for such errors without needing specialized navigators or trajectory measurement sequences to aid the reconstruction.

A known limitation of spiral sampling is its sensitivity to off-resonance artifacts, which can manifest as signal loss/blurring artifacts at various air-tissue interfaces (e.g., at the lips, tongue, velum in dynamic speech imaging [3]). This effect is more pronounced at high field strengths (>3 T) and with the use of long readouts. While the effect can be reduced by using short readout spirals, this will result in reduced time acquisition efficiency. Several deblurring methods exist that rely on dual TE acquisitions to estimate the time-varying field map [4] or employ nonconvex autofocus metrics [5, 6] to correct for off-resonance-induced distortions. More recently, a single TE-based dynamic off-resonance correction scheme has been proposed [2], and in the context of dynamic speech MRI, has shown to be effective at improving articulator sharpness. One example of this scheme in spiral speech 3 T data

(A) without correction   (B) with correction (MUSSELS)
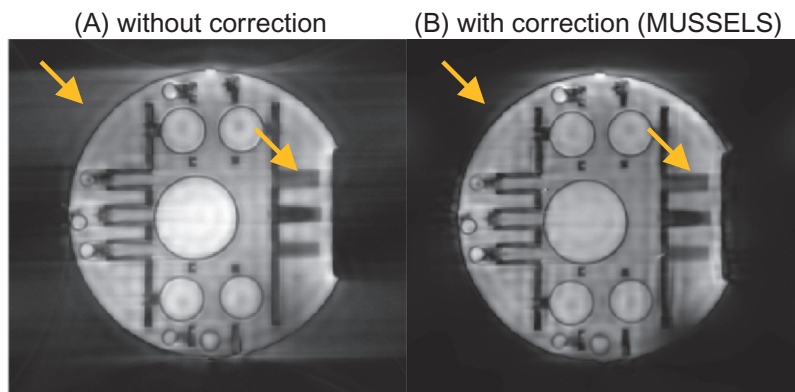
FIG. 18.3

Need for trajectory error correction in radial acquisitions: (A) an uncorrected image of a phantom reconstructed with the designed radial trajectory. Since the scanner executed trajectory did not match the designed trajectory, significant geometric distortions in the image exist (see *arrows* in (A) highlighting blurring, and smearing artifacts). (B) The result of a trajectory mismatch correction algorithm, which reconstructed the same raw data via a structured low-rank matrix completion model-based algorithm [1] without needing additional calibration measurements.

Courtesy: Merry Mani, University of Iowa.
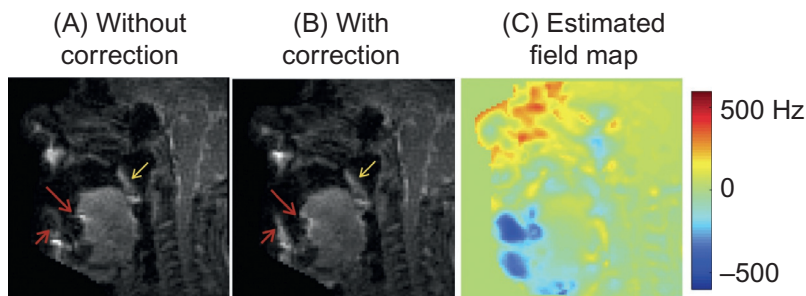
FIG. 18.4

Long readout spiral acquisitions are challenged by off-resonance artifacts. This example shows a speech MR image in the midsagittal plane acquired using a 3.0 ms long spiral readout at 3 T. Due to the long readout length, significant blurring at air-tissue interfaces is seen in (A). These can be mitigated via off-resonance correction algorithms. (B) The reconstruction output of a single TE-based off-resonance correction algorithm [2], which estimates the field map in (C) and uses it to correct for off-resonance-induced blurring (see improved sharpness at the *arrows* near the lower lip, tongue tip, velum in (A), (B)).

is shown in Fig. 18.4. It can be seen that jointly estimating the time-varying field map and using it in the reconstruction can correct for some of the off-resonance-induced blurring at various air-tissue interfaces (e.g., at the lips, tongue tip, velum).

## 18.3 Parallel imaging and generalized spatiotemporal models

We will consider the problem of recovering dynamic dataset $\gamma(\mathbf{x}, t)$ from sparsely sampled k-t noisy measurements $b(\mathbf{k}, t)$. The problem can be compactly written in the vector form as

$$b(\mathbf{k}, t) = \mathcal{A}(\gamma(\mathbf{x}, t)) + n(\mathbf{k}, t), \tag{18.1}$$

where the operator $\mathcal{A}$ models for the coil sensitivity encoding as well as Fourier encoding on a specified k-t sparse sampling trajectory. $n(\mathbf{k}, t)$ may be modeled as additive Gaussian noise.

18.3.1 Parallel imaging

Parallel imaging methods solve the above problem by exploiting the spatial diversity of the receiver coil sensitivities (e.g., SENSE [7], GRAPPA [9], ESPIRIT [10], ENLIVE [8]). The most important factor with any parallel imaging method is on the assumptions being made, while modeling/estimating coil sensitivities. If the object moves, it is important to reestimate/recalibrate coil maps for accurate modeling of the parallel imaging problem. Fig. 18.5i shows a simulated brain MR imaging example of a 2×2 SENSE reconstruction, where coil maps calibrated in one position are used during reconstruction of the brain moved to a different position. This example shows considerable reconstruction artifacts due to incorrect coil maps. In scenarios where the receiver array coil jointly moves with the object (e.g., flexible chest array coils for cardiac, or abdomen imaging), it is imperative to jointly estimate the coil maps along with the reconstruction. Fig. 18.5ii shows an example demonstrating
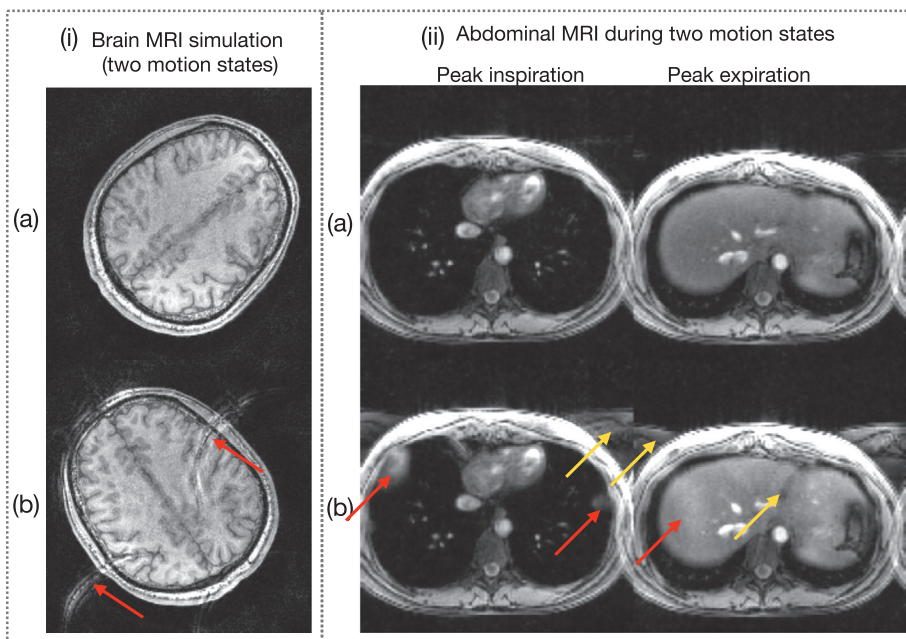
FIG. 18.5

Effects of motion in parallel imaging. (i) Brain MR imaging simulations in two motion states from a 2×2 SENSE reconstruction [7]. Both reconstructions used the same set of coil maps, which were derived when the brain was in the motion state of (i)(a). Artifacts due to incorrect usage of coil maps are thus observed in (i)(b) (see *red arrows*). (ii) An abdominal MR imaging experiment in two motion states of peak inspiration, and peak expiration at rate 2 undersampling using ENLIVE [8]. Note in this experiment, the receiver coil physically touches the body, and moves together with the body. (ii)(a) The reconstructions with joint estimation of the coil maps along with the reconstructions. However, if the coil maps were swapped, one can appreciate the severity of artifacts in incorrectly using coil maps from different motion states (e.g., false structures, and intensity shading; see *yellow and red arrows*, respectively, in (ii)(b)).

Courtesy: Martin Uecker, Graz University of Technology.

abdominal MR imaging during inspiration and expiration at rate 2 undersampling by the ENLIVE parallel imaging approach [8]. The top row shows reconstructions, where the coil maps are jointly estimated along with the reconstructions for each of the inspiration, and expiration phases. The bottom row shows the same data but reconstructed with swapped coil sensitivities. This shows significant artifacts in the form of intensity shading, and false structure-like artifacts (see arrows in Fig. 18.5ii).

While parallel MR-based methods can achieve moderate acceleration factors to improve dynamic imaging, their performance is typically limited by the coil geometry, and associated g-factor noise amplification at high acceleration factors. In the following sections, we will discuss models that exploit spatiotemporal redundancies in the dataset, and are complementary to parallel MR imaging.

18.3.2 Generalized spatiotemporal models

Various spatiotemporal models have been proposed in the past to model the temporal dynamics (including motion) in the dynamic dataset [11–19]. These can be interpreted in an unified manner by the generalized partial separability (PS) model [14], where a global signal model is used to represent the signal time profile at each voxel ($\gamma(\mathbf{x}, t)$) as

$$\gamma(\mathbf{x}, t) = \sum_{i=1}^{R} u_i(\mathbf{x}) v_i(t). \tag{18.2}$$

The above decomposition decomposes $\gamma(\mathbf{x}, t)$ as a product of the spatial model coefficients $u_i(\mathbf{x})$ and the temporal basis functions $v_i(t)$. Here, R denotes the total number of basis functions (or the model order). The model in Eq. (18.2) can be represented in a matrix form, where the dynamic Casorati matrix ($\mathbf{\Gamma}_{M \times N}$) can be decomposed as a product of a spatial coefficient matrix $\mathbf{U}_{M \times R}$ and a matrix $\mathbf{V}_{R \times N}$ containing the temporal basis functions:

$$\underbrace{\begin{pmatrix} \gamma(\mathbf{x}_1, t_1) & . & . & . & \gamma(\mathbf{x}_1, t_N) \\ \gamma(\mathbf{x}_2, t_1) & . & . & . & \gamma(\mathbf{x}_2, t_N) \\ . & & . & & . \\ . & & . & & . \\ \gamma(\mathbf{x}_M, t_1) & . & . & . & \gamma(\mathbf{x}_M, t_N) \end{pmatrix}}_{\mathbf{\Gamma}_{M \times N}} = \underbrace{\begin{pmatrix} u_1(\mathbf{x}_1) & . & . & u_R(\mathbf{x}_1) \\ u_1(\mathbf{x}_2) & . & . & u_R(\mathbf{x}_2) \\ . & & . & . \\ . & & . & . \\ u_1(\mathbf{x}_M) & . & . & u_R(\mathbf{x}_M) \end{pmatrix}}_{\mathbf{U}_{M \times R}} \underbrace{\begin{pmatrix} v_1(t_1) & . & . & v_1(t_N) \\ v_2(t_1) & . & . & v_2(t_N) \\ . & & . & . \\ v_R(t_1) & . & . & v_R(t_N) \end{pmatrix}}_{\mathbf{V}_{R \times N}}. \tag{18.3}$$

Here, M represents the number of voxels per frame, and N denotes the number of time frames. Based on the constraints imposed on the matrices $\mathbf{U}$, $\mathbf{V}$, and the number of basis functions R, the general PS model in Eq. (18.3) can be classified into various models as laid out in Fig. 18.6.
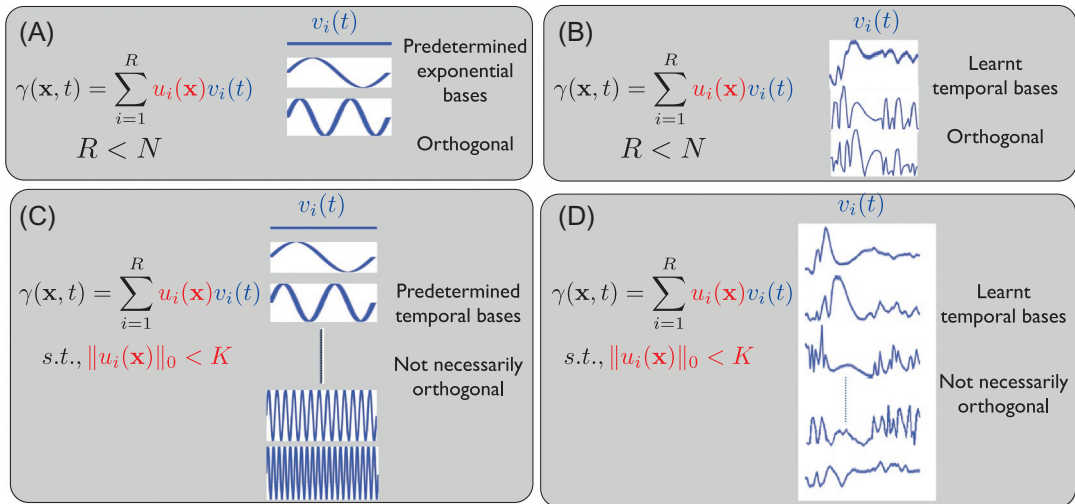

FIG. 18.6

Generalized partial separability model [14] decomposition for (A) linear models, (B) blind linear models (low-rank models), (C) compressed sensing under synthesis representation, and (D) blind compressed sensing.

In applications such as breath-held cardiac cine MRI, or functional MRI, where the temporal dynamics are quasiperiodic, $\gamma(\mathbf{x}, t)$ can be modeled as linear combination of few exponential temporal basis functions (i.e., $R < N$, and these basis functions represent the fundamental frequency of the motion along with its harmonics). Therefore, the generalized PS model simplifies to

$$\gamma(\mathbf{x}, t) = \sum_{i=1}^{R} u_i(\mathbf{x})e^{j2\pi f t}; R < N. \tag{18.4}$$

The above may be viewed as a *linear model* with predetermined choice of few exponential temporal basis functions to model temporal dynamics (including motion). Schemes such as DIME [11], UNFOLD [12], and k-t BLAST [13], assume the above linear model. The k-t sampling patterns are designed in a specialized manner (e.g., lattice sampling pattern in Fig. 18.1a) so that the alias artifacts overlap in a highly structured manner in the spatial domain versus temporal frequency space (or the so-called x-f space). This model assumes that the x-f space is highly structured with limited significant components. However, this assumption breaks down with significant nonperiodic interframe motion such as breathing motion in free-breathing ungated cardiac cine MRI (also see Fig. 18.7).

Compressed sensing (CS) under the synthesis basis representation models $\gamma(\mathbf{x}, t)$ as a sparse linear combination of temporal basis functions from a predetermined overcomplete dictionary (e.g., wavelet bases, complex exponential bases). Therefore, synthesis-based CS can be viewed with the generalized PS model as
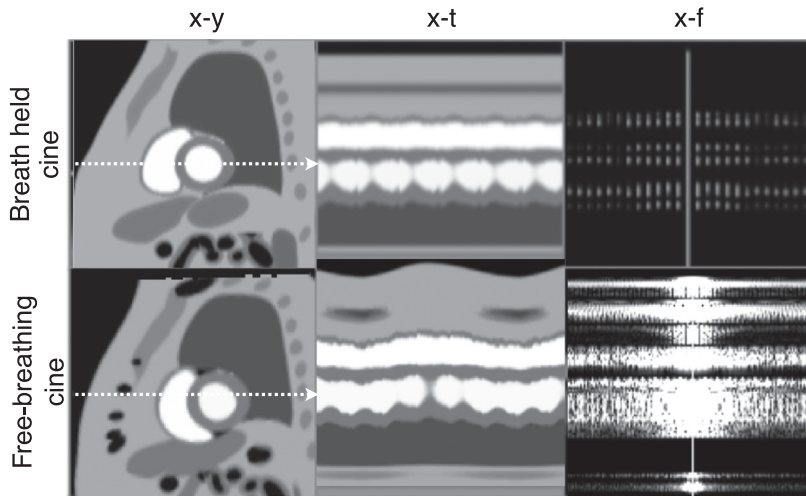

FIG. 18.7

Motion representation in the spatial-spectral (x-f) space. Shown here are short-axis 2D cardiac MRI phantom simulations of breath-held cine imaging (*top row*), and free-breathing cine imaging (*bottom row*). The image time profiles in the second column through the chambers of the heart reveal the motion dynamics. The periodicity of the beating heart in breath-held cine translates to a highly structured/sparse representation in the (x-f) space. However, in the presence of breathing motion (*second row*), the structure/sparsity in the x-f space is highly disturbed due to the requirement of more exponential harmonics to accurately model the breathing motion.

$$\gamma(\mathbf{x}, t) = \sum_{i=1}^{R} u_i(\mathbf{x}) \underbrace{v_i(t)}_{\text{Predetermined dictionary}} \quad ; R > N$$

$$\text{such that } \|u_i(\mathbf{x})\|_0 < K,$$

(18.5)

where $\|\cdot\|_0$ represents the l_0 norm operator that enforces sparsity on $u_i(\mathbf{x})$. K indicates the sparsity level, which represents the number of basis functions selected from the dictionary for modeling a single-voxel time profile. The other key difference in CS compared to linear models is that it relies on k-t sampling patterns that result in incoherent/random alias artifacts, and uses iterative nonlinear optimization algorithms for reconstruction. CS using exponential bases as the dictionary also has similar challenges as linear models when modeling nonperiodic arbitrary motion as the assumption of sparsity in the x-f space breaks down.

Low-rank methods model $\gamma(\mathbf{x}, t)$ as a linear combination of few orthogonal learned temporal basis functions [14, 16, 17, 19]. The basis functions can be obtained from the singular value decomposition of the Casorati matrix ($\mathbf{\Gamma}$).

$$\gamma(\mathbf{x}, t) = \sum_{i=1}^{R} u_i(\mathbf{x}) \underbrace{v_i(t)}_{\text{From SVD}} \quad ; R < N.$$

(18.6)

The low-rank model can be imposed in several ways. The two-step strategy [14, 16] estimates the temporal bases from low spatial but high-temporal resolution training data, and the associated spatial weights $u_i(\mathbf{x})$ are obtained by regularized least square fitting with the undersampled k-space measurements. Single-step methods jointly estimate $u_i(\mathbf{x})$ and $v_i(t)$ from the undersampled measurements. For example, the method of k-t SLR [17] (exploiting low rank and sparsity of the dynamic data) uses spectral penalties such as nuclear norm or Schatten p-norm to enforce the low-rank constraint, and uses an iterative low-rank matrix recovery algorithm to solve the resulting reconstruction optimization. Since the temporal bases are learned from the data itself, they capture the motion patterns in the dynamic data. However, it is important to note that for accurate modeling of all the motion components, a higher rank is often needed, which directly restricts the full power of low-rank approaches for highly accelerated imaging. To illustrate this, Fig. 18.8 shows the singular value decay plot of the $\mathbf{\Gamma}$ matrix in dynamic speech MRI, where the subject is performing three tasks (a) stationary with a dry swallow; (b) repeated utterance of consonants and vowels sounds (za-na-za); and (c) producing spontaneous speech with no repetitions. It is seen that the resulting rank of $\mathbf{\Gamma}$ gets progressively higher as the complexity of the motion patterns increases.

Blind compressed sensing (BCS) models $\gamma(\mathbf{x}, t)$ as a sparse linear combination of temporal basis functions from a learned dictionary [18]. The basis functions need not be orthogonal as in low-rank models. BCS can be viewed as

$$\gamma(\mathbf{x}, t) = \sum_{i=1}^{R} u_i(\mathbf{x}) \underbrace{v_i(t)}_{\text{Learned dictionary}} \quad ; R > N$$

$$\text{such that } \|u_i(\mathbf{x})\|_0 < K.$$

(18.7)

Since BCS uses an overcomplete learned dictionary, it has more degrees of freedom to model arbitrary motion patterns occurring simultaneously at different voxels. Therefore, the main advantage of BCS over classical CS and low-rank models is its ability to model arbitrary motion patterns. It should be noted that BCS schemes are often sensitive to learning arbitrary noise patterns in the basis functions. This can interfere in interpretation of the underlying true motion of the object [20].
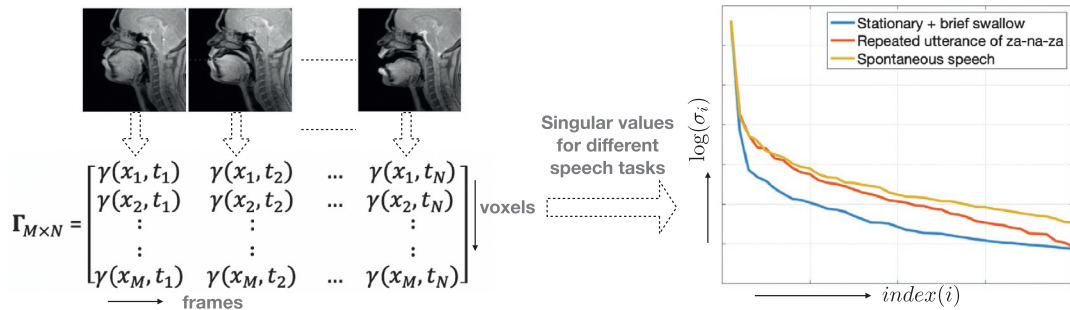
FIG. 18.8

Rank of the Casorati matrix $\mathbf{\Gamma}$ is dependent on the complexity of motion. Shown here are the singular value decay plots for three different speech tasks: stationary + brief swallow task, utterance of za-na-za sound, and spontaneous speech. As the complexity of the motion increases, the rate of singular value decay gets slower (or the rank increases).

18.4 Explicit motion estimation and motion-compensated reconstruction

All the generalized spatiotemporal models discussed in the previous section are sensitive to large inter-frame motion. To address this, there have been several schemes that jointly estimate the interframe motion and reconstruction, which targeting the spatiotemporal redundancy of the motion-compensated dynamic dataset [21–26]. Fig. 18.9 shows a representation of a free-breathing myocardial perfusion PINCAT phantom [22] without and with breathing motion correction. Compared to the original dataset, the motion-compensated dataset has smoother pixel time profiles, which make it suited for temporal
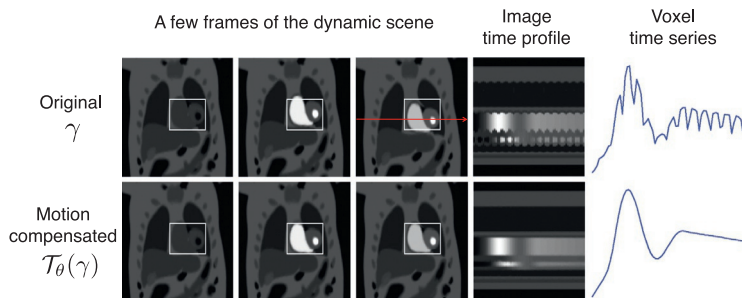

FIG. 18.9

Free-breathing myocardial perfusion MR imaging data with and without deformation correction: Example dynamic frames from a myocardial perfusion PINCAT MR phantom that contains considerable interframe breathing motion is shown in the *top row*. The corresponding deformation/motion corrected dataset is shown in the *bottom row*. A *square box* is superimposed on the heart to better visualize the motion of the heart due to breathing. The image time profiles of the original and deformation due to motion correction datasets along the *red arrow* are also shown. The ripples in the time profile in the *top row* correspond to the motion. The corresponding deformation corrected profile in the *bottom row* shows that profile is largely free of the ripples. The voxel time profiles are more piecewise smooth with the deformation corrected data compared to the original, hence the former has more sparse temporal gradients.

finite difference-based compressed sensing. In addition, the motion-compensated dataset will also have a much more compact x-f space representation and a lower rank compared to the original dataset.

One example formulation for explicit motion estimation and compensated reconstruction is shown below:

$$\min_{\gamma(\mathbf{x},t),\,\theta(\mathbf{x},t)} \|A(\gamma) - \mathbf{b}\|_2^2 + \lambda\psi(\mathcal{T}_\theta(\gamma)) + \mu\mathcal{R}(\theta), \tag{18.8}$$

where $\theta(\mathbf{x}, t)$ represents the spatial deformation maps characterizing motion at time frame t. The first term ensures data consistency. The second term enforces a compactness prior (ψ) on the motion-compensated dataset $\mathcal{T}_\theta(\gamma)$. ψ is the operator that exploits spatiotemporal redundancy. Some examples may be sparsity under the temporal Fourier transform $\psi(\cdot) = \|\mathcal{F}_t(\cdot)\|_1$; sparsity after the temporal finite difference operation $\psi(\cdot) = \|\nabla_t(\cdot)\|_1$; or the nuclear norm operator exploiting the global low-rank structure. The third term is a regularization functional on the deformation maps, which typically enforce spatial smoothness on θ (e.g., Gaussian-based regularizers).

Fig. 18.10 shows an example comparison of ultrashort echo time (UTE) free-breathing pulmonary MR without and with motion-compensated reconstruction, against reference high-resolution computed
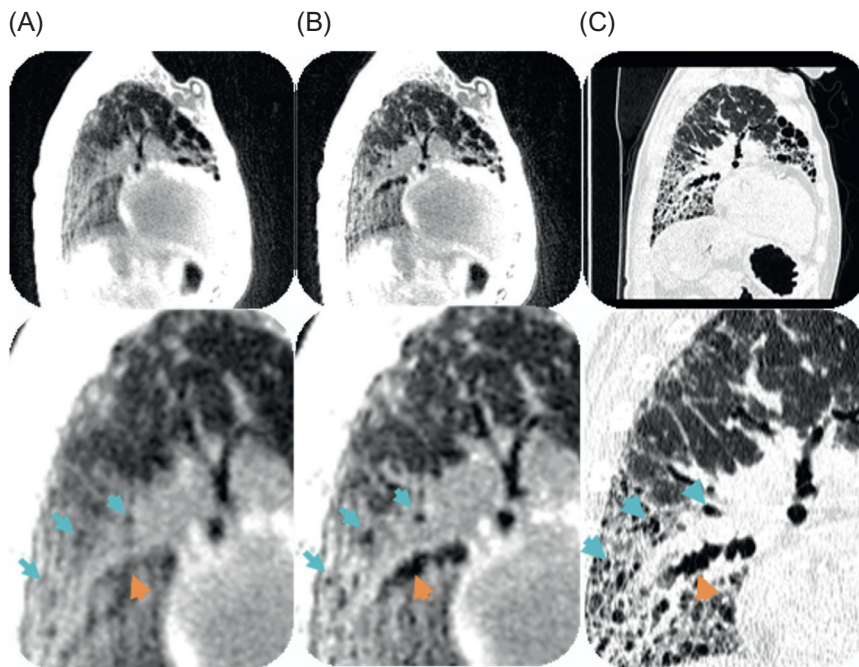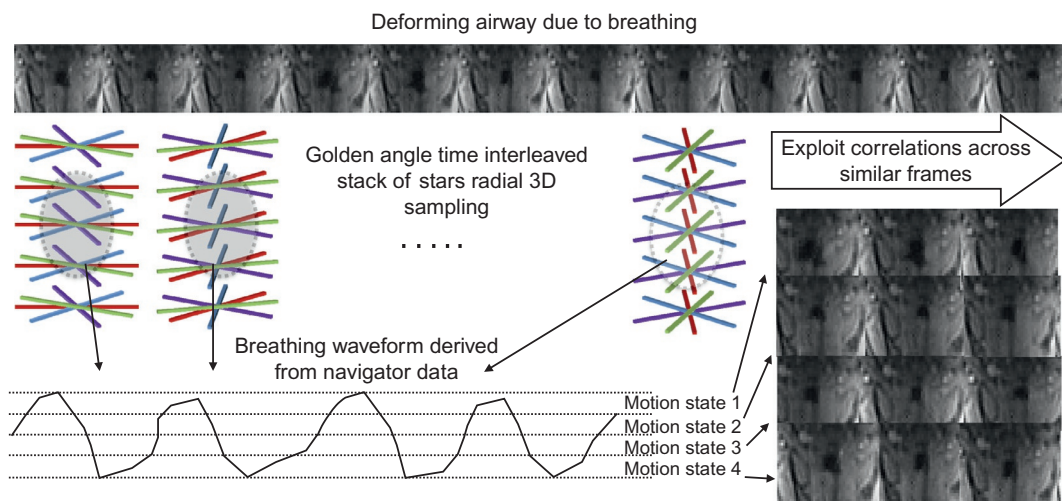

FIG. 18.10

Example reconstruction quality of explicit motion estimation and compensation strategy. Shown here is a sagittal slice of an idiopathic pulmonary fibrosis patient with severe honeycombing (*blue arrows*) and traction bronchiectasis (*orange arrows*). Iterative MoCo is an approach that jointly estimates the deformation and imposes sparsity on the motion-compensated dataset. It resolves CT-like features with less blurring and improved contrast compared to classical constrained reconstruction without motion compensation. (A) No compensation, (B) iterative MoCo, and (C) high-resolution CT.

Courtesy: Luis Torres, University of Wisconsin, Madison; and Sean Fain, University of Iowa.

tomography (CT). This figure shows a scan from an idiopathic pulmonary fibrosis patient, whose lung parenchyma shows the typical pattern of honeycombing and interstitial fibrosis (as seen in the high-resolution CT image). Iterative MoCo is an approach that jointly estimates the deformation maps and the reconstruction [26, 27]. Spatiotemporal sparsity is promoted on the motion-compensated dataset. In contrast to classical compressed sensing reconstruction (without motion compensation), iterative MoCo is able to resolve texture content (such as honeycombing and traction bronchiectasis).

18.5 Implicit motion-compensated reconstruction

While the above explicit motion estimation and motion-compensated reconstruction schemes are powerful in minimizing motion artifacts in spatiotemporal constrained reconstruction, they are practically challenged with nonconvexity, and are therefore sensitive to local minima. Moreover, given the joint estimation of motion maps, the total memory demands and the reconstruction time increase dramatically, which is a challenge especially while handling large 3D + time datasets. To address these limitations, several implicit motion-resolved reconstruction schemes have evolved [28–31]. These are based on using information from navigator signals that capture major motion patterns. The navigators can be obtained from external measuring probes such as respiratory bellows, or derived from the k-space data itself. Fig. 18.11 shows a schematic of one such approach using a stack of stars radial

FIG. 18.11

Extra dimension regularization-based schemes extract major motion patterns from the data itself, and use it to bin the dynamic data into image frames with similar motion states. Shown here is imaging of the deforming airway in the axial plane. The airway space shown is behind the tongue at the oropharynx level and is zoomed in for improved visualization of the airway shape change due to motion. A stack of stars radial sequence is used for concept illustration. The central k-space data are used as a navigator data to extract the breathing waveform, which then can be used to bin the dynamic data into image frames with similar motion states. Finally, sparsity/structure along this new dimension can be enforced to exploit similarity between frames with similar shapes, thus achieving implicit motion compensation without explicit estimation of the deformation maps.

sequence. The central low-resolution k-space can be used to extract the underlying 1D respiratory-induced motion. Once this is extracted, the dynamic data can be binned to similar respiratory motion states, thereby inducing an *extra* dimension. The reconstruction then involves exploiting sparsity/structure along this new dimension, which implicitly does motion compensation without explicitly estimating the motion maps. An example reconstruction formulation exploiting sparsity under the temporal finite difference operation (∇_t) is shown below:

$$\min_{\gamma(\mathbf{x}, t)} \|A(\gamma) - \mathbf{b}\|_2^2 + \lambda \|\nabla_t(S(\gamma))\|_1, \tag{18.9}$$

where S is an operator that resizes γ that has M voxels per frame and N time frames as $(M)(n_{bins}) \times (n\, frames_{bin})$, where n_{bins} represent the number of bins that represent different respiratory motion states, and number of frames per bin represents an auxiliary fifth dimension that contains the number of time phases in each motion state ($= N/n\, frames_{bin}$).

Besides resolving motion, the extra-dimensional class of methods can resolve mixing imaging effects due to complex coupling among different dynamic physiological processes (e.g., change of respiratory phase will also affect cardiac phase). Hence, interdependency of the individual dynamic processes can be learned, which is not possible with classical spatiotemporal models.

18.6 Manifold regularization

If there is excessive motion in the object, then the Casorati matrix may not be sufficiently low in rank. However, in dynamic MR imaging, it is often observed that there is repetition of similar images. These similar images do not necessarily occur periodically in time. To exploit this property, manifold learning (ML) methods have been introduced, where sets of similar images can be recovered efficiently [32–34].

Images $\gamma(\mathbf{x}, t_1), \gamma(\mathbf{x}, t_2), \ldots, \gamma(\mathbf{x}, t_N)$ can be modeled as points on a low-dimensional manifold (a smooth surface) in a high-dimensional ambient space with dimension equal to total pixels M in each image. This assumption holds true if there is high similarity amongst these images. For example, in the application of free-breathing ungated cardiac cine MR, the images can be associated with the nonlinear functions of two parameters: the cardiac and respiratory phases. Images with similar cardiac and respiratory phases are expected to be comparable; and hence will be mapped as neighbors on the manifold. Similarly, in an application of dynamic speech MR with an arbitrary speaking task, even though the task is not repeating, similar posture frames will be efficiently mapped as neighbors on the manifold. Fig. 18.12 demonstrates this concept on a simulated speech phantom [35], where similar but distant time frames are mapped to lie in close proximity on the smooth manifold.

Manifold regularization exploits the similarity of image frames in terms of the proximity of the points on the smooth manifold. The reconstruction can be written as

$$\min_{\gamma} \|\mathcal{A}(\gamma) - \mathbf{b}\|_2^2 + \lambda \sum_{i=1}^{N} \sum_{j=1}^{N} w_{ij} \|\gamma_i - \gamma_j\|_2^2. \tag{18.10}$$

The weights w_{ij} determine the degree of similarity between the ith and the jth frame; and are inversely proportional to the distance between the corresponding points on the manifold. If the frames are similar (e.g., similar postures in speech MR imaging), then w_{ij} will be assigned a higher weight, and vice versa. The weights are learned from the data itself, and one strategy is to use low-resolution central k-space data $b_{low\, res}(\mathbf{k}, t)$ as navigator signals to estimate the weights as
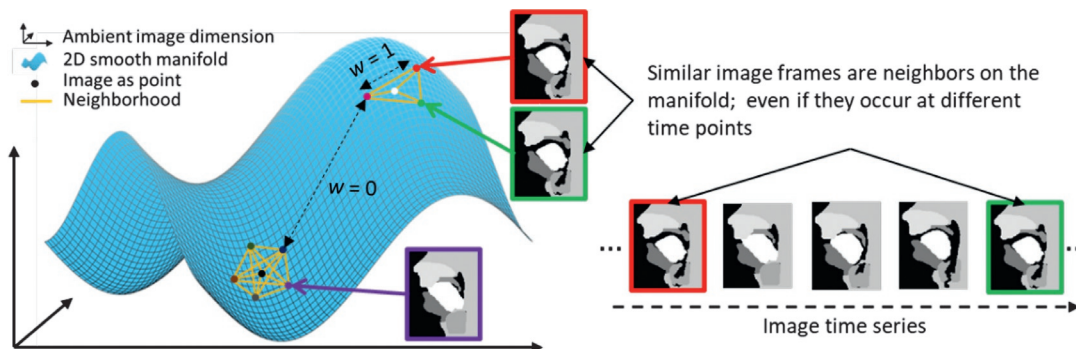
FIG. 18.12

Schematic demonstration of mapping of image frames onto a smooth manifold. Image frames are modeled as points on a smooth manifold surface in a higher-dimensional space. Similar images will be mapped as neighbors ($w = 1$) on the manifold, while dissimilar images ($w = 0$) are separated far away on the manifold. The manifold mapping thus efficiently allows for exploiting redundancies between similar frames even if they occur distant in time.

$$w_{ij} = \begin{cases} e^{-\frac{\|\gamma_i - \gamma_j\|_2^2}{\sigma^2}}, & \text{if } \|\gamma_i - \gamma_j\|_2^2 < 2\sigma, \\ 0, & \text{otherwise.} \end{cases} \qquad (18.11)$$

Here, σ is a parameter that depends on the maximum curvature on the manifold, and is a free parameter to be optimized by the user.

Manifold learning schemes are powerful in applications involving nonperiodic, arbitrary motion, where heuristic-based binning strategies would fail. An example application is dynamic speech imaging, where kinematics of several articulators (e.g., lips, tongue, soft palate) are often arbitrary. Fig. 18.13 shows an example result in this application comparing the reconstruction quality of the manifold regularization scheme against temporal finite difference-based compressed sensing, and low-rank regularized reconstructions. Since the manifold learning scheme implicitly learns similarity between distant image frames even in the presence of aperiodic motion, it depicts robust spatiotemporal fidelity. In contrast, the low-rank and temporal finite difference schemes demonstrate spatial and temporal blurring artifacts.

18.7 Need for validation studies

This chapter discussed various linear and nonlinear methods to reconstruct the underlying dynamic object from sparsely sampled acquisitions. Linear methods such as parallel imaging, and view sharing typically operate at lower acceleration rates. However, they allow for quantitative characterization of reconstruction quality (e.g., via analysis of point spread functions, g-factor maps). Nonlinear methods have emerged, and are continually being adapted for several highly accelerated dynamic imaging applications. One of the major challenges associated with these nonlinear models is the characterization of nontrivial reconstruction artifacts, which are introduced based on the assumptions being made in these models. To address this, comprehensive application-specific validation studies are needed.
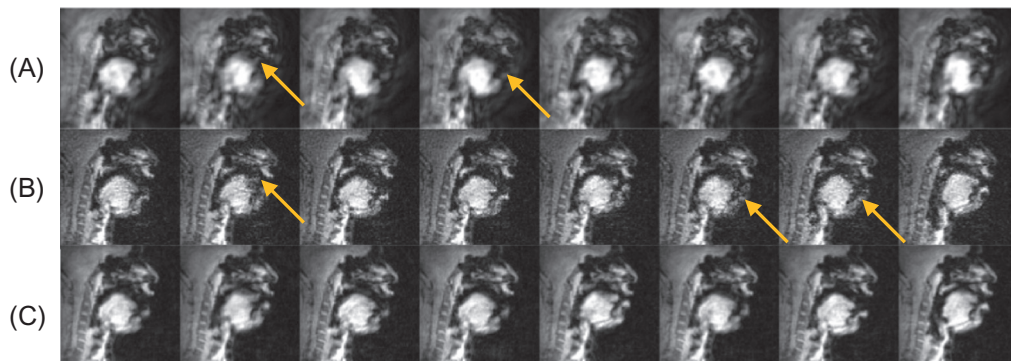
FIG. 18.13

Example comparison of manifold regularization against low-rank and temporal finite difference regularization schemes. Shown here is an example that compares slice two, obtained in the sagittal plane, of a three-slice dynamic speech MR dataset while the subject was uttering the phrase "za-na-za." Considerable spatiotemporal blurring artifacts are observed in the low-rank and temporal finite difference reconstructions (see *yellow arrows*). In contrast, manifold learning has good spatiotemporal fidelity and preserves the motion of articulators well, due to its ability to identify similar image frames even if they occur distantly in time. (A) Low rank, (B) temporal finite difference, and (C) manifold.

Validation based on physical moving phantoms with known velocities has been used in the past [36]. Methods that use human observer models to validate reconstruction image quality from a task detection perspective have been recently developed [37]. Validation against alternate modalities such as CT have been performed [27]. The field is actively moving toward blinded image quality evaluation from clinical expert end users in different categories such as assessment of spatial blurring, temporal blurring, loss of contrast/features in important structures, and alias artifacts [38–42]. Competitions organized by international societies continue to evolve as an avenue to compare various emerging reconstructions from a task detection perspective [43]. In summary, the need for such validation studies represents a crucial bottleneck in the routine clinical implementation of nonlinear reconstruction models for highly accelerated dynamic imaging.

References

[1] Mani M, Magnotta V, Jacob M. A general algorithm for compensation of trajectory errors: application to radial imaging. Magn Reson Med 2018;80(4):1605–13.

[2] Lim Y, Lingala SG, Narayanan SS, Nayak KS. Dynamic off-resonance correction for spiral real-time MRI of speech. Magn Reson Med 2019;81(1):234–46.

[3] Lingala SG, Sutton BP, Miquel ME, Nayak KS. Recommendations for real-time speech MRI. J Magn Reson Imaging 2016;43(1):28–44.

[4] Sutton BP, Conway CA, Bae Y, Seethamraju R, Kuehn DP. Faster dynamic imaging of speech with field inhomogeneity corrected spiral fast low angle shot (flash) at 3 T. J Magn Reson Imaging 2010;32 (5):1228–37.

[5] Smith TB, Nayak KS. Automatic off-resonance correction in spiral imaging with piecewise linear autofocus. Magn Reson Med 2013;69(1):82–90.

[6] Chen W, Meyer CH. Fast automatic linear off-resonance correction method for spiral imaging. Mag Reson Med 2006;56(2):457–62.

[7] Pruessmann KP, Weiger M, Börnert P, Boesiger P. Advances in sensitivity encoding with arbitrary k-space trajectories. Magn Reson Med 2001;46(4):638–51. https://doi.org/10.1002/mrm.1241.

[8] Holme HCM, Rosenzweig S, Ong F, Wilke RN, Lustig M, Uecker M. ENLIVE: an efficient nonlinear method for calibrationless and robust parallel imaging. Sci Rep 2019;9(1):1–13.

[9] Griswold MA, Jakob PM, Heidemann RM, Nittka M, Jellus V, Wang J, et al. Generalized autocalibrating partially parallel acquisitions (GRAPPA). Magn Reson Med 2002;47(6):1202–10.

[10] Uecker M, Lai P, Murphy MJ, Virtue P, Elad M, Pauly JM, et al. ESPIRiT—an eigenvalue approach to auto-calibrating parallel MRI: where SENSE meets GRAPPA. Magn Reson Med 2014;71(3):990–1001.

[11] Liang ZP, Jiang H, Hess CP, Lauterbur PC. Dynamic imaging by model estimation. Int J Imaging Syst Technol 1997;8(6):551–7.

[12] Tsao J. On the UNFOLD method. Magn Reson Med 2002;47(1):202–7.

[13] Tsao J, Boesiger P, Pruessmann KP. k-t BLAST and k-t SENSE: dynamic MRI with high frame rate exploiting spatiotemporal correlations. Magn Reson Med 2003;50(5):1031–42.

[14] Liang ZP. Spatiotemporal imaging with partially separable functions. In: 2007 4th IEEE international symposium on biomedical imaging: from nano to macro. IEEE; 2007. p. 988–91.

[15] Jung H, Sung K, Nayak KS, Kim EY, Ye JC. k-t FOCUSS: a general compressed sensing framework for high resolution dynamic MRI. Magn Reson Med 2009;61(1):103–16.

[16] Pedersen H, Kozerke S, Ringgaard S, Nehrke K, Kim WY. k-t PCA: temporally constrained k-t BLAST reconstruction using principal component analysis. Magn Reson Med 2009;62(3):706–16.

[17] Lingala SG, Hu Y, DiBella E, Jacob M. Accelerated dynamic MRI exploiting sparsity and low-rank structure: kt SLR. IEEE Trans Med Imaging 2011;30(5):1042–54.

[18] Lingala SG, Jacob M. Blind compressive sensing dynamic MRI. IEEE Trans Med Imaging 2013;32 (6):1132–45.

[19] Christodoulou AG, Zhang H, Zhao B, Hitchens TK, Ho C, Liang ZP. High-resolution cardiovascular MRI by integrating parallel imaging with low-rank and sparse modeling. IEEE Trans Biomed Eng 2013;60 (11):3083–92.

[20] Lingala SG, Jacob M. Blind compressed sensing with sparse dictionaries for accelerated dynamic MRI. In: 2013 IEEE 10th international symposium on biomedical imaging. IEEE; 2013. p. 5–8.

[21] Usman M, Atkinson D, Odille F, Kolbitsch C, Vaillant G, Schaeffter T, et al. Motion corrected compressed sensing for free-breathing dynamic cardiac MRI. Magn Reson Med 2013;70(2):504–16.

[22] Lingala SG, DiBella E, Jacob M. Deformation corrected compressed sensing (DC-CS): a novel framework for accelerated dynamic MRI. IEEE Trans Med Imaging 2014;34(1):72–85.

[23] Chen X, Salerno M, Yang Y, Epstein FH. Motion-compensated compressed sensing for dynamic contrast-enhanced MRI using regional spatiotemporal sparsity and region tracking: block low-rank sparsity with motion-guidance (BLOSM). Magn Reson Med 2014;72(4):1028–38.

[24] Royuela-del-Val J, Usman M, Cordero-Grande L, Martin-Fernandez M, Simmross-Wattenberg F, Prieto C, et al. Whole-heart single breath-hold cardiac cine: a robust motion-compensated compressed sensing reconstruction method. In: Reconstruction, segmentation, and analysis of medical images. Springer; 2016. p. 58–69.

[25] Royuela-del-Val J, Cordero-Grande L, Simmross-Wattenberg F, Martín-Fernández M, Alberola-López C. Jacobian weighted temporal total variation for motion compensated compressed sensing reconstruction of dynamic MRI. Magn Reson Med 2017;77(3):1208–15.

[26] Zhu X, Chan M, Lustig M, Johnson KM, Larson PEZ. Iterative motion-compensation reconstruction ultra-short TE (iMoCo UTE) for high-resolution free-breathing pulmonary MRI. Magn Reson Med 2020;83 (4):1208–21.

[27] Torres LA, et al. Motion compensation in pulmonary ultra-short echo time MRI: preliminary results in id-iopathic pulmonary fibrosis. In: Proceedings of the international society for magnetic resonance in medicine; 2020. p. 7117.

[28] Feng L, Axel L, Chandarana H, Block KT, Sodickson DK, Otazo R. XD-GRASP: golden-angle radial MRI with reconstruction of extra motion-state dimensions using compressed sensing. Magn Reson Med 2016;75 (2):775–88.

[29] Chitiboi T, Muckley M, Dane B, Huang C, Feng L, Chandarana H. Pancreas deformation in the presence of tumors using feature tracking from free-breathing XD-GRASP MRI. J Magn Reson Imaging 2019;50 (5):1633–40.

[30] Feng L, Coppo S, Piccini D, Yerly J, Lim RP, Masci PG, et al. 5D whole-heart sparse MRI. Magn Reson Med 2018;79(2):826–38.

[31] Cheng JY, Zhang T, Alley MT, Uecker M, Lustig M, Pauly JM, et al. Comprehensive multi-dimensional MRI for the simultaneous assessment of cardiopulmonary anatomy and physiology. Sci Rep 2017;7(1). https://doi. org/10.1038/s41598-017-04676-8.

[32] Poddar S, Jacob M. Dynamic MRI using smoothness regularization on manifolds (SToRM). IEEE Trans Med Imaging 2015;35(4):1106–15.

[33] Nakarmi U, Wang Y, Lyu J, Liang D, Ying L. A kernel-based low-rank (KLR) model for low-dimensional manifold recovery in highly accelerated dynamic MRI. IEEE Trans Med Imaging 2017;36(11):2297–307.

[34] Ahmed AH, Zhou R, Yang Y, Nagpal P, Salerno M, Jacob M. Free-breathing and ungated dynamic MRI using navigator-less spiral storm. IEEE Trans Med Imaging 2020;39(12):3933–43.

[35] Martin J, Ruthven M, Boubertakh R, Miquel ME. Realistic dynamic numerical phantom for MRI of the upper vocal tract. J Imaging 2020;6(9):86.

[36] Frahm J, Schätz S, Untenberger M, Zhang S, Voit D, Merboldt KD, et al. On the temporal fidelity of nonlinear inverse reconstructions for real-time MRI—the motion challenge. Open Med Imaging J 2014;8:1–7.

[37] Pineda AR, Miedema H, Lingala SG, Nayak KS. Optimizing constrained reconstruction in magnetic reso-nance imaging for signal detection. Phys Med Biol 2021;66(14):145014.

[38] Yang ACY, Kretzler M, Sudarski S, Gulani V, Seiberlich N. Sparse reconstruction techniques in MRI: methods, applications, and challenges to clinical adoption. Invest Radiol 2016;51(6):349.

[39] Vasanawala SS, Alley MT, Hargreaves BA, Barth RA, Pauly JM, Lustig M. Improved pediatric MR imaging with compressed sensing. Radiology 2010;256(2):607–16.

[40] Guo Y, Lebel RM, Zhu Y, Lingala SG, Shiroishi MS, Law M, et al. High-resolution whole-brain DCE-MRI using constrained reconstruction: prospective clinical evaluation in brain tumor patients. Med Phys 2016;43 (5):2013–23.

[41] Fushimi Y, Okada T, Kikuchi T, Yamamoto A, Okada T, Yamamoto T, et al. Clinical evaluation of time-of-flight MR angiography with sparse undersampling and iterative reconstruction for cerebral aneurysms. NMR Biomed 2017;30(11):e3774.

[42] Lu SS, Qi M, Zhang X, Mu XH, Schmidt M, Sun Y, et al. Clinical evaluation of highly accelerated com-pressed sensing time-of-flight MR angiography for intracranial arterial stenosis. Am J Neuroradiol 2018;39(10):1833–8.

[43] Muckley MJ, Riemenschneider B, Radmanesh A, Kim S, Jeong G, Ko J, et al. State-of-the-art machine learn-ing MRI reconstruction in 2020: results of the second fastMRI challenge. arXiv preprint arXiv:201206318: 2020.